Soft Matter

PAPER

Cite this: *Soft Matter*, 2021, **17**, 3234

Dissipative non-equilibrium dynamics of self-assembled paramagnetic colloidal clusters†

Mohammed Elismaili, Lydiane Bécu, Hong Xu and David Gonzalez-Rodriguez

Received 17th December 2020,
Accepted 4th February 2021

DOI: 10.1039/d0sm02218g

rsc.li/soft-matter-journal

We study experimentally and theoretically the dynamics of two-dimensional clusters of paramagnetic colloids under a time-varying magnetic field. These self-assembled clusters are a dissipative non-equilibrium system with shared features with aggregates of living matter. We investigate the dynamics of cluster rotation and develop a theoretical model to explain the emergence of collective viscoelastic properties. The model successfully captures the observed dependence on particle, cluster, and field characteristics, and it provides an estimate of cluster viscoelasticity. We also study the rapid cluster disassembly in response to a change in the external field. The experimentally observed disassembly dynamics are successfully described by a model, which also allows estimating the particle–substrate friction coefficient. Our study highlights physical mechanisms that may be at play in biological aggregates, where similar dynamical behaviors are observed.

1 Introduction

Inert systems spontaneously evolve towards equilibrium states, corresponding to absolute minima of the free energy, or towards kinetically trapped states, corresponding to local minima. Living systems, however, often operate in dissipative nonequilibrium states by continuously consuming energy.[1–3] Dissipative nonequilibrium endows living systems with a remarkable adaptability to their environment. Whereas equilibrium states are often associated with permanent properties, such as the structural color of bird feathers, dissipative nonequilibrium states enable on-demand changes, such as the active structural color of the chameleon.[4]

A physically intriguing type of living system is the assembly of interacting subunits, such as birds, fish, ants, bacteria, or cells. For example, cellularised materials are assemblies of cells linked by intercellular junctions that are found in embryonic tissues or in pathologies such as tumors.[5] These different types of biological aggregates exhibit emergent collective mechanical behavior, whose origin is a combination of the mechanical properties of the subunits as well as of their interactions. Both the properties and interactions of the subunits rely on active, energy-consuming processes. Understanding the emergence of the collective mechanical properties of biological aggregates is a major current challenge in biophysics.[5] Physical investigations of such biological systems often rely on analogies with model systems in soft matter,[6] such as colloidal aggregates. Conversely, the versatility of biological materials, which are able to switch from fluid-like swarms to viscoelastic materials that sustain force, and from dynamical aggregation to disassembly, is a rich source of inspiration for the development of new colloidal materials.[7]

The model system investigated in this article is a two-dimensional assembly of paramagnetic colloids under an external, rotating magnetic field. The self-assembly of paramagnetic colloids has attracted significant attention in recent years. Whereas self-assembly under a static magnetic field has been extensively studied,[8–14] recent developments have focused on self-assembly under time-dependent fields.[15,42] A time-dependent, three-dimensional magnetic field can be implemented by a system of Helmholtz coils.[16] By varying the field orientation and frequency, various structures, such as chains, ribbons, membranes, networks, foams, or vortices, are formed.[15,17–22] Colloidal suspensions under such complex magnetic fields exhibit dynamics reminiscent of locomotion, swarming, or feeding in living systems, which has been resumed by saying that complex fields breathe life into colloidal suspensions.[23] An additional element of complexity is introduced by colloidal interactions with liquid or solid interfaces,[24] as is the case in our study.

When paramagnetic colloids on a 2D substrate are subjected to a static magnetic field, either contained in the plane of the substrate (tilt angle $\theta = 90^\circ$) or at a tilt angle larger than the so-called magic angle, they aggregate into chains. As an external rotating field of progressively increasing precession frequency is applied, the chains first rotate with the field, then deform under the action of viscous fluid forces, and eventually

Université de Lorraine, LCP-A2MC, F-57000, Metz, France.
E-mail: mohammed.el-ismaili@univ-lorraine.fr, lydiane.becu@univ-lorraine.fr, hong.xu@univ-lorraine.fr, david.gr@univ-lorraine.fr

† Electronic supplementary information (ESI) available. See DOI: 10.1039/d0sm02218g

consolidate into isotropic, disk-like clusters.[25–27] The rotation of magnetic particles and clusters is governed by a balance between viscous resistance and magnetic torque, the ratio of which is called the Mason number. As the precession frequency increases, the Mason number increases, and the viscous resistance prevents single magnetic particles from following the rotation of the field. Thus, single particles first transition from rotation to wobbling, and at large enough precession frequencies they stop rotating.[28] A similar behavior is observed for the rotation of particle chains stabilized by chemical bonding.[29] In contrast with single particles and permanent chains, isotropic particle clusters rotate even at high field precession frequencies, albeit their rotation frequency becomes slower than that of the external field. In the case of clusters of Janus particles, the rotation at high precession frequencies is driven by hydrodynamic interactions.[30] A different mechanism, led by viscoelastic shear waves of cluster deformation, can explain the rotation of clusters of isotropic magnetic particles at high precession frequency.[26] Here, we investigate these viscoelastic cluster dynamics, which reproduce several key features of biological aggregates: first, viscoelasticity emerges as a collective phenomenon that does not simply reflect the mechanical properties of individual constituents; second, viscoelasticity is a dissipative nonequilibrium phenomenon that requires a continuous energy input; and third, clusters are reversible structures that disassemble upon changes in the external field. Magnetic particle clusters under a time-varying field are thus a model system that allows both mimicking and interpreting dissipative self-assembly mechanisms that are ubiquitous in nature.

In this article we study the dynamics of the rotation of isotropic paramagnetic particle clusters, the emergence of viscoelastic properties, and cluster disassembly upon modification of the external field. Building upon the pioneering work of Tierno and collaborators, who investigated 7-particle hexagonal clusters,[26] here we study paramagnetic clusters of various sizes and particle types, under external magnetic fields of various intensities and frequencies. We start by describing our experimental system of study. Then, we derive two separate, analytical theoretical models to explain the dynamics of cluster's rotation and disassembly. Each of the two models has a single fitting parameter. By comparing the models' predictions to our experimental observations, we evaluate the two parameters and obtain estimates of collective cluster viscoelasticity and of substrate friction.

2 Materials and methods

2.1 Experimental setup

The experimental setup consists of two pairs of Helmholtz coils with their main axes contained in the horizontal plane, and a simple coil with a vertical axis surrounding the others. The three coil axes are arranged perpendicular to each other (Fig. 1(a)), which allows generation of a 3D rotating magnetic field $\mathbf{B} = (B\sin\theta\cos(2\pi\Omega t), B\sin\theta\sin(2\pi\Omega t), B\cos\theta)$, where B is the induced magnetic field strength, Ω is the precession frequency, and t is the elapsed time (Fig. 1(b)). The whole setup

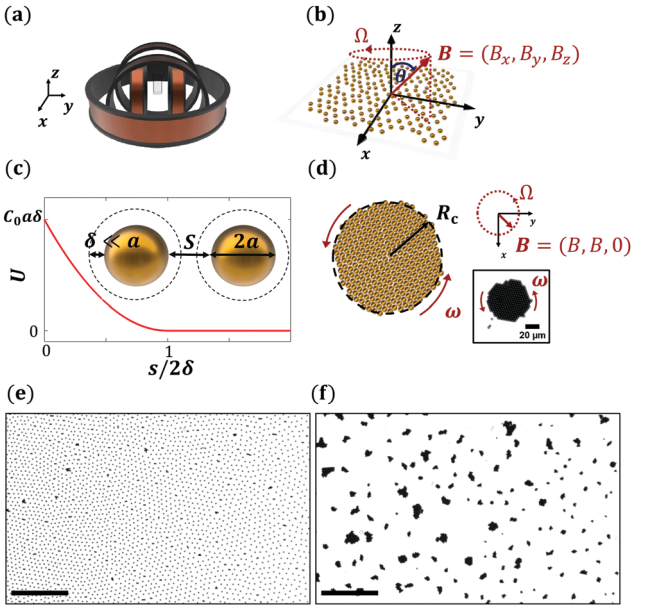

Fig. 1 (a) Schematic diagram of the experimental setup. (b) Sketch of an ensemble of paramagnetic particles located on the sample plane xy at the bottom of the sample cell. The particles are exposed to a magnetic field $\boldsymbol{B}$ that rotates with a precession frequency Ω over the surface of a cone of tilt angle θ. (c) Steric potential between two particles coated with a layer of SDS molecules of width δ and separated by a surface-to-surface distance s (see the text). (d) Schematic representation of a quasi-circular cluster of radius R_c. Driven by the in-plane rotating magnetic field, the cluster rotates with an angular velocity ω. The inset shows an experimental image of an actual rotating cluster. (e and f) Two microscope images (the scale bar is 200 μm) of a mono-dispersed layer of particles M-450 (e) before application of the magnetic field and (f) 580 seconds after applying an external in-plane rotating magnetic field (θ = 90°; B = 1 mT; Ω = 2960 Hz).

is built on the stage of an inverted microscope equipped with a CCD camera.

2.2 Sample preparation

We use two types of super-paramagnetic polystyrene particles, Dynabeads M-450 and Dynabeads M-270, of radius a_1 = 2.2 μm and a_2 = 1.4 μm, and dimensionless magnetic susceptibilities χ_1 = 1.632 and χ_2 = 0.756, respectively.[31] A direct experimental estimation of particle susceptibilities is presented in the ESI† and in the Fig. S1 (ESI†) therein. Particles are suspended in a sodium dodecyl sulfate (SDS) solution with a concentration of 2.1 g L^{-1}. The SDS molecules are adsorbed onto the particle surface and prevent spontaneous aggregation and particle binding to the substrate. Before starting the experiment, particles are allowed to sediment at the bottom of the sample quartz cell (Hellma Analytics) placed at the center of the triple coil setup. A weak, vertical magnetic field (B = 0.5 mT) is exerted to distribute particles over the 1 cm × 1 cm sample cell bottom, where a particle array of a surface density of (2.15 ± 0.35) × 10^{-3} particles per μm^2 is obtained.

2.3 Experimental protocol

First, we investigate the rotation dynamics of 2D self-assembled colloidal clusters. A 2D monodisperse particle array (Fig. 1(e)) is

placed under an in-plane ($\theta = 90^\circ$) rotating magnetic field. This planar field generates dipolar attractive interactions among the magnetized particles, which causes particle self-assembling into 2D rotating clusters of different sizes (Fig. 1(d and f) and Movie S1, ESI†). We set as our baseline experimental conditions $B = 1$ mT and $\Omega = 660$ Hz, using Dynabeads M-450 as particles. By varying one parameter at a time, we examine how the angular rotation velocity of the cluster, ω, depends on the characteristics of the magnetic field (Ω and B) and on the particle type (with different a and χ).

Second, we investigate the dynamics of cluster disassembly. Once clusters are formed under the action of an in-plane rotating field, the second experiment starts by imposing a constant vertical magnetic field in the z-direction ($B = 0.9$ mT, $\theta = 0^\circ$). The vertical field induces repulsive interactions between the cluster's particles, which causes their spreading. Both the rotation and disassembly dynamics are monitored with the CDD camera at an image rate of 5 frames per second (Movie S2, ESI†).

2.4 Data analysis

The image files are processed using ImageJ (Fiji)[32] to obtain the size, position, and orientation of clusters. A customized code is used to track the clusters. The instantaneous angular velocity of a cluster, ω, is determined from the variation in the cluster orientation between consecutive frames. To obtain meaningful values of ω, the calculation is restricted to clusters that are sufficiently large and stable over time, according to the following criteria: (i) cluster size above 80 μm^2, (ii) variation of cluster size less than 5%, (iii) cluster trajectory recorded during at least 12 s, and (iv) standard deviation of ω smaller than 0.05 rev s^{-1}.

To quantify the dynamics of cluster disassembly, the particle closest to the cluster barycenter at the beginning of the experiment is identified as the central particle and assumed to remain as such. The experimental local density profile during cluster disassembly is obtained as $\rho(r_i) = 2/\left[\sqrt{3}/d(r_i)^2\right]$, where $d(r_i)$ is the average distance between a particle located at the radial distance r_i from the cluster center and its six nearest neighbors. To account for boundary effects, the distance d for particles at the cluster's edge is calculated as the average distance to its three nearest neighbors only, and a factor of 1/2 is applied to the resulting density ρ. The cluster radius $R(t)$ is that of the circle circumscribing all the cluster's particles.

3 Theoretical models

3.1 Dynamics of cluster rotation

The rotation of self-assembled 2D paramagnetic clusters in a rapidly precessing magnetic field with a tilt angle above the magic angle was first studied by Tierno *et al.*[26] for small hexagonal clusters consisting of 7 particles. At high precession frequency, cluster rotation was theoretically explained by the dynamics of dissipative elastic shear waves traveling around the cluster.[26] However, as discussed in Section 4, this hexagonal cluster model is not directly applicable to our experiments including a variety of cluster sizes, as its predictions fail to describe the dynamics we observe. Taking the hexagonal cluster model as our starting point, we develop an extended theoretical model that captures the new physics in our experiments.

Cluster self-assembly is driven by the time-averaged dipolar interactions between the time-varying magnetic dipoles induced by the rotating field. The equilibrium particle positions in the cluster are determined by a balance between these attractive interactions and the short-range repulsive steric interactions arising from the SDS molecules adsorbed onto the particle's surface (Fig. 1(b)). At high precession frequency Ω of the external magnetic field, the particle's dipole orientation cannot follow the field rotation, and single particles do not rotate. In contrast, clusters rotate, although at a lower speed than the external field. The mechanism of cluster rotation is not due to dipole rotation, nor does it require an anisotropic cluster shape. Rather, rotation of isotropic clusters is enabled by dynamic deformation driven by the imbalance of magnetic forces at the cluster's edge. By using a continuum description, which is valid for clusters containing a sufficiently high number of particles, magnetic forces acting at the edge of the two-dimensional cluster can be expressed as a dipolar line tension, with units of force, given by $\lambda_{dip} = \lambda_{is} + \lambda_{anis}\cos(2\Phi)$, where Φ is the in-plane angle between the magnetic field and the vector normal to the cluster boundary, $\boldsymbol{n}$.[26] The isotropic component λ_{is} assures cluster cohesion, whereas the anisotropic component λ_{anis} induces cluster deformation. As in previous work,[26] we conceptualize the cluster as a 2D incompressible viscoelastic solid, whose deformation is described by the elasticity equation $-\boldsymbol{\nabla} p + G_c \Delta \boldsymbol{u} = 0$, where G_c is the complex shear modulus, and $p > 0$ is the steric pressure. By solving the elasticity equation subjected to the boundary condition that the elastic stress normal to the boundary is caused by the dipolar line tension gradient, the following expression of the radial component of the dynamic cluster deformation is obtained:[26]

$$u_r = \frac{-2\lambda_{anis} R_c}{3(\lambda_{is} + G_c R_c)} \exp(-2i\Phi)\ , \qquad (1)$$

where R_c is the cluster radius.

The rotating magnetic field exerts a magnetic torque $\tau_m = V_c B^2 \sin^2(\theta)\chi_{eff}''/\mu_0$ on the cluster, where V_c is the cluster volume, μ_0 is the vacuum permeability, and χ_{eff}'' is the imaginary part of the magnetic susceptibility, $\chi_{eff}'' = 3\pi a u_r''/8R_c^2$, where a is the particle radius.[26] Cluster rotation is opposed by a viscous torque $\tau_{visc} = f\eta_w R_c^3 \omega$, where η_w is the viscosity of water, and $f = A\pi R_c \omega^{1/2}/2\nu_w^{1/2}$ is the dimensionless hydrodynamic drag coefficient of the cluster, assimilated to a rotating flat disk near a wall, with ν_w the kinematic viscosity of water and A a numerical constant that depends on the disk roughness ($A = 0.6159$ for a flat, impervious disk).[33] Unlike previous modeling work,[26] we do not simplify the hydrodynamic drag as that of a collection of non-interacting spheres, but rather we consider the drag due to the actual cluster shape.

Cluster viscoelasticity is described by the Kelvin–Voigt model, $G_c = K - 2i(\Omega - \omega)\eta_c$, where K is the 2D elastic modulus (with units of force per length) and η_c is the 2D cluster viscosity

(with units of force–time per length). Thus, the radial distortion becomes (see the ESI† for details):

$$u_r = \frac{-2\lambda_{anis} R_c[(\lambda_{is} + KR_c) + 2i(\Omega - \omega)\eta_c R_c]}{3\left[(\lambda_{is} + KR_c)^2 + (2(\Omega - \omega)\eta_c R_c)^2\right]} \exp(-2i\Phi). \quad (2)$$

At this point we diverge again from previous work on hexagonal clusters,[26] which assumed a cluster elasticity proportional to the isotropic surface tension, $K = \lambda_{is}/R_c$. If we applied this hypothesis to our larger clusters, we would predict a radial cluster deformation of the order of 50%, much larger than what is observed experimentally. Rather, we postulate that the dominant contribution to the storage shear modulus arises from steric interactions. The steric interaction potential (Fig. 1(c)) between two identical particles of radius a, with a coating layer of width δ and separated by a surface-to-surface distance s is:[34]

$$U = \begin{cases} C_0 a^2 \left(2 - \frac{l}{q} - \frac{l+2}{q} \ln \frac{1+q}{1+l/2}\right) & \text{if } l \le 2q, \\ 0 & \text{if } l > 2q, \end{cases} \quad (3)$$

where $C_0 \equiv 2\pi\Gamma k_B T$, k_B is the Boltzmann constant, T is the temperature, Γ is the so-called grafting density, *i.e.*, the surface density of molecules adsorbed onto the particle surface, $s = r - 2a$, with r the center-to-center distance, $l \equiv s/a$, and $q \equiv \delta/a$. Since $q \ll 1$, we can simplify the steric potential expression for $l \le 2q$ as: $U \approx C_0 a^2 \left(q - l + \frac{l^2}{4q}\right)$.

The 2D elastic modulus K of the cluster is then deduced as follows. If we apply a pressure p_c along the cluster edge, the cluster radius is reduced by a magnitude $|\Delta R_c| = \int_a^{R_c} \varepsilon(r) dr$, so that $p_c a = K|\Delta R_c|/R_c$. The local deformation at radius r due to the pressure $p(r) = p_c R_c/r$ is $\varepsilon(r) = ap(r)/(d^2U/dr^2)$. Thus, we obtain $K = Ca/\ln(R_c/a)$, with $C \equiv C_0/(2\delta)$.

By balancing the magnetic and viscous torques and by considering that $\Omega \gg \omega$, $\lambda_{is} \ll KR_c$, and $\eta_c\Omega \ll K$, we obtain the cluster's angular velocity:

$$\omega = \gamma \ln^{2/3}\left(\frac{2^{5/2}}{3^{1/4}e^{7/3}} \frac{R_c}{a}\right) \ln^{4/3}\left(\frac{R_c}{a}\right) \frac{(a\chi)^{4/3}}{R_c^{8/3}} \Omega^{2/3} B^{8/3}, \quad (4)$$

with $\gamma \equiv \left[\frac{4\pi^2}{18A\mu_0^2} \frac{\sqrt{\nu_w}}{\eta_w} \frac{\eta_c}{C^2} \sin^4\theta\right]^{2/3}$.

Let us analyze eqn (4) by considering only the dominant power-law dependencies. The equation predicts the cluster's angular velocity to approximately depend on cluster size as $\omega \propto R_c^{-8/3}$, on particle properties as $\omega \propto (a\chi)^{4/3}$, and on magnetic field frequency and intensity as $\omega \propto \Omega^{2/3}B^{8/3}$. In contrast, the earlier hexagonal cluster model[26] predicted a different dependence on field precession frequency and particle susceptibility, $\omega \propto \Omega/\chi^2$, a weak (logarithmic) dependence on R_c/a, and it predicted ω to be independent of B. We note that our predicted dependence of ω on particle size arises from assuming that particle repulsion is dominated by steric interactions. A similar result would be obtained for electrostatic repulsion. Indeed, the electrostatic repulsion potential between two particles of radius a at an interparticle distance s scales as $U \propto a\exp(-\kappa s)$, where κ^{-1} is the Debye length. Therefore, the 2D elastic modulus would scale as $K \sim \partial^2 U/\partial s^2 \propto a$, which is the same dependence as obtained for steric interactions. Therefore, the predicted parameter dependences are robust, independent of whether interparticle repulsion is dominated by steric or electrostatic interactions.

The parameters present in eqn (4) can all be determined from the characteristics of our experimental setup, except for one single fitting parameter, η_c/C^2. Fitting this viscoelastic parameter to the experimental data allows estimating the magnetic cluster's viscosity, η_c.

3.2 Disassembly dynamics

We now consider the dynamics of disassembly of a cluster subjected to a static magnetic field perpendicular to the cluster plane. Two previous studies investigated this phenomenon through experiments and numerical simulations, describing pattern formation[35] and quantifying the early dynamics, where particles lose contact with each other.[36] Here we present a closed-form analytical model able to describe the long-term dynamics (see the ESI† for additional details of the derivation). We consider the spatio-temporal variation of the density profile, $\rho(r,t)$, defined as the number of particles per unit area. We adopt a mean-field approach to write the conservation equation of the particle number,

$$\frac{\partial \rho}{\partial t} + v\frac{\partial \rho}{\partial r} = -\rho\left(\frac{v}{r} + \frac{\partial v}{\partial r}\right), \quad (5)$$

where v is the radial velocity of particles, related to the interparticle magnetic force F by $v = \frac{F}{\xi}$, where ξ is the particle–substrate friction coefficient. In the mean-field approach, the dipolar potential energy depends on the local density by $U_{dip} = \frac{2M}{5}\frac{\mu_0}{4\pi}\chi_V^2 B^2 \rho(r,t)^{3/2}$, where $\chi_V = \chi V_p/\mu_0$ with $V_p = 4\pi a^3/3$ the particle volume, and $M \approx 11.116$ is a geometrical constant obtained by the sum of dipolar interactions among all particles in an hexagonal lattice.[14] Thus we obtain the particle velocity $v = -\frac{\rho^{1/2}}{\beta}\frac{\partial \rho}{\partial r}$, with $\beta = \frac{20\pi\xi}{3M\mu_0\chi_V^2 B^2}$. Eqn (5) becomes:

$$\beta\frac{\partial \rho}{\partial t} = \rho^{3/2}\frac{\partial^2 \rho}{\partial r^2} + \frac{1}{r}\rho^{3/2}\frac{\partial \rho}{\partial r} + \frac{3}{2}\rho^{1/2}\left(\frac{\partial \rho}{\partial r}\right)^2, \quad (6)$$

with boundary conditions $\partial\rho/\partial r = 0$ at $r = 0$ and $\rho(R) = 0$, where R is the cluster radius (note that $R(t = 0) = R_c$). To solve eqn (6), we assume that the density profile can be factorized as $\rho(r,t) = \rho_0(t)y(x)$, where $\rho_0(t) = \rho(0,t)$ is the density at the cluster center, and $x = r/R(t)$ is the dimensionless radial distance. The conservation law of the total number of particles N yields:

$$\rho_0(t) = \frac{N}{\pi I}\frac{1}{R(t)^2},$$

where $I \equiv \int_0^1 2y(x)x\mathrm{d}x$. Therefore, eqn (6) can be written as:

$$-2\beta\left(\frac{\pi I}{N}\right)^{3/2} R^4 \frac{\mathrm{d}R}{\mathrm{d}t} = \left[y^{1/2}y'' + y^{1/2}\frac{y'}{x} + \frac{3}{2}y^{-1/2}(y')^2\right]\left[1 + \frac{xy'}{2y}\right]^{-1} = -\alpha, \tag{7}$$

where α is a separation constant and y' and y'' are respectively the first and second derivatives of $y(x)$. The exact solution for the temporal factor in eqn (7) is:

$$R(t)^5 = R_c^5 + \frac{5\alpha}{2\beta}\left(\frac{N}{\pi I}\right)^{3/2} t, \tag{8}$$

whereas the exact solution for the spatial factor is:

$$y(x) = (1 - x^2)^{\alpha/4}, \tag{9}$$

with $\alpha = 8/3$.

The model's eqn (8) predicts an evolution of the cluster radius R such that R^5 increases linearly with t. This result contains one single fitting parameter, which is the particle–substrate friction coefficient ξ, contained in the parameter β. Thus, by fitting eqn (8) to the experimentally observed cluster radius evolution, the model allows estimating ξ. Moreover, the model predicts that the spatial density structure of the cluster follows a normalized master curve given by eqn (9).

4 Results and discussion

4.1 Rotation of self-assembled clusters

4.1.1 Dependence on cluster size and magnetic field frequency. In our experiments, we observe that for a sufficiently high precession magnetic field frequency, particles self-assemble into rotating 2D clusters with different sizes (see Movie S1, ESI†). The angular velocity of the cluster, ω, depends on the cluster's area A_c, *i.e.*, on the number of particles forming the cluster, and on the magnetic field frequency Ω. Fig. 2(a) shows that smaller clusters rotate faster, and that the cluster's angular velocity increases with the precession magnetic field frequency. Fig. 2(b) shows the angular velocity of clusters normalized according to eqn (4) and demonstrates that the experiments are well described by our theoretical model. The prediction is best for larger clusters, where our model's continuum approximation is fully appropriate.

By fitting the model's single parameter to the experiments, we obtain a cluster viscoelastic ratio $\eta_c/C^2 = 5.6 \times 10^{-14}$ N s m^{-1} Pa^{-2}. To further characterize the viscoelastic properties, we need to estimate C, related to cluster elasticity arising from steric interactions. Because the value of C is very sensitive to the nanoscale characteristics of the particle coating, whose accurate determination is difficult, we proceed by a direct measurement of cluster elasticity. We measure cluster deformation when the field increases from $B = 0.5$ mT to $B = 1$ mT. The pressure exerted on the cluster depends on B through the isotropic component of the line tension, $p_c = \lambda_{is}/(4\pi R_c a)$. By measuring the resulting decrease in cluster radius $|\Delta R_c|$, the cluster elasticity can be estimated from the previously stated relationship, $|\Delta R_c| = \int_a^{R_c} \varepsilon(r)\mathrm{d}r$. This leads to an estimate of the elasticity coefficient $C = \frac{a\chi^2}{108\mu_0}\ln(1.58Rc/a)\ln(Rc/a)$ $\Delta(B^2)/|\Delta R_c| = 7.7 \pm 1.0$ Pa and to an estimate of the 2D cluster viscosity $\eta_c = (3.5 \pm 0.6) \times 10^{-12}$ N s m^{-1}, a comparable value to previously reported magnetic cluster viscosity measurements.[26]

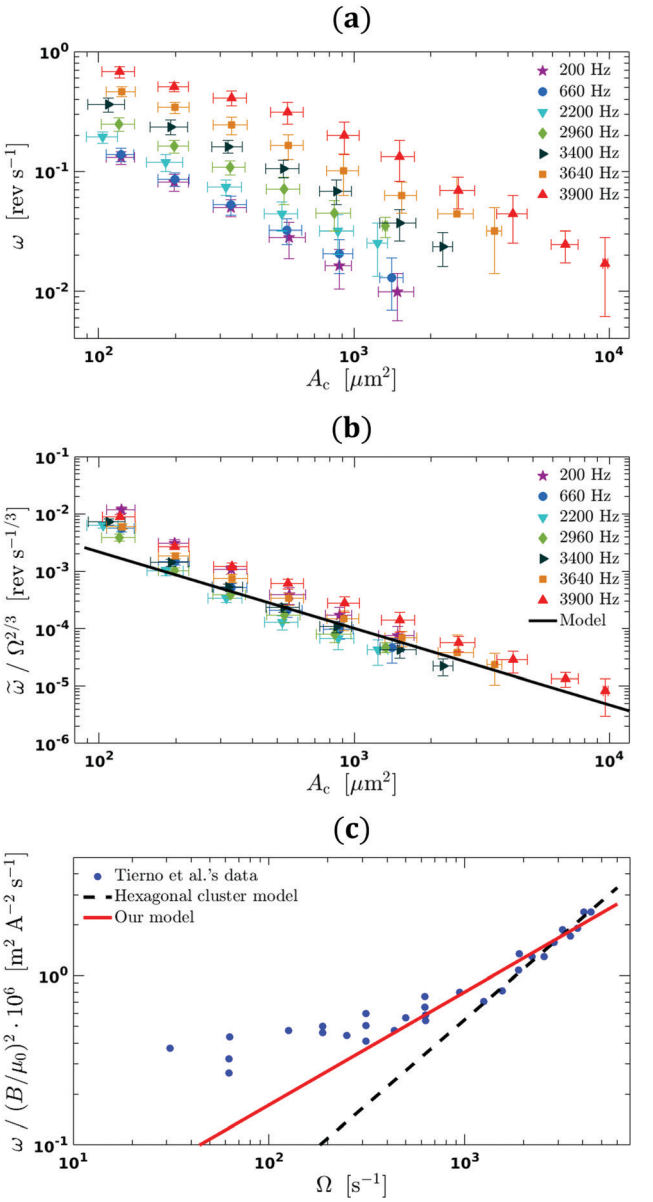

Fig. 2 (a) Angular velocity of cluster rotation ω as a function of cluster area A_c at different magnetic field frequencies Ω. Experiments are performed with M-450 particles and $B = 1$ mT. (b) Normalized angular velocity $\tilde{\omega}/\Omega^{2/3}$, with $\tilde{\omega} = \omega \ln^{-2/3}\left(\frac{2^{5/2}}{3^{1/4}e^{7/3}}\frac{R_c}{a}\right)\ln^{-4/3}\left(\frac{R_c}{a}\right)$. The continuous black line is a fit using eqn (4). (c) Normalized cluster rotation frequency of a rotating hexagon of seven particles as a function of Ω for $\theta = 90°$, as reported by Tierno *et al.*[26] The dashed black line represents the scaling predicted by Tierno *et al.* ($\omega \propto \Omega$), and the full red line is a fit to Tierno *et al.*'s data using eqn (4). Error bars in plots (a) and (b) are standard deviations over 5 experiments.

In Fig. 2(b), we note that the collapse between the data corresponding to different Ω, while satisfactory, is not perfect. However, the scaling dependence predicted by our model $\omega \propto \Omega^{2/3}$ performs much better than the prediction of the hexagonal cluster model, $\omega_{\mathrm{Hex}} \propto \Omega$, both when applied to our data and to the previously published hexagonal cluster data[26] (Fig. 2(c)). In Fig. 2(c) we observe that both our model and the earlier hexagonal model[26] correctly predict the hexagonal data at large precession frequencies but not at lower ones. Indeed, at precession frequencies lower than about 100 s^{-1}, the magnetic susceptibility tensor of the cluster becomes anisotropic,[26] inducing faster rotation than the viscoelastic deformation mechanism considered in our model.

4.1.2 Dependence on magnetic field strength. Fig. 3(a) shows the cluster angular velocity ω as a function of its area A_c for Ω = 660 Hz for three different magnetic field strengths, B = 0.5, 1, and 2 mT. The hexagonal cluster model predicts an ω independent of B and thus cannot account for the observed dependence. In contrast, our model's eqn (4) predicts the scaling $\omega \propto B^{8/3}$. Fig. 3(b) shows that the experimental curves of ω normalized according to eqn (4) collapse with each other, and an excellent agreement between theory and experiments is found, especially for larger clusters. We also performed experiments at a larger field strength (B = 3 mT, not shown). For $B \geq 3$ mT, magnetic forces may overcome gravity and we observe the formation of clusters with vertically superimposed particles, a configuration that is no longer described by our theory.

4.1.3 Dependence on particle characteristics. Fig. 4 compares the dynamics of clusters of two different particle types, Dynabeads M-270 and M-450. M-270 particles have a smaller size and a smaller magnetic susceptibility than M-450 particles. We observe that an M-270 cluster rotates slower than an M-450 cluster of the same size. Fig. 4(a) shows the dependence between ω and A_c for the two particle types. In Fig. 4(b) the results are normalized according to the dependence on particle size a and susceptibility χ predicted by eqn (4). When normalized by our prediction, for large clusters the two curves collapse into a master curve that is in excellent agreement with the prediction of our mean-field model.

4.2 Disassembly dynamics

Upon application of a vertical magnetic field ($\theta = 0^\circ$), the cluster disassembles and spreads. A quasi-triangular lattice was observed with a local density ρ depending on radial position r and time t. Fig. 5(a) shows experimental snapshots for a cluster of 47 particles exposed to a magnetic field of strength B = 0.9

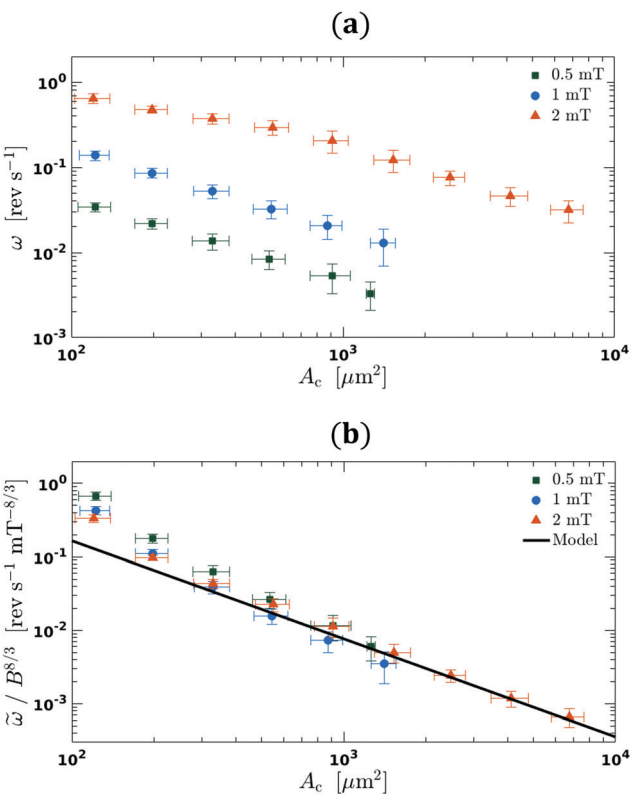

Fig. 3 (a) Cluster angular velocity ω as a function of cluster area A_c (M-450; Ω = 660 Hz) at three different magnetic field intensities B. (b) Normalized cluster angular velocity $\tilde{\omega}/B^{8/3}$ as a function of A_c. The continuous black line is a fit using eqn (4). Error bars are standard deviations over 5 experiments.

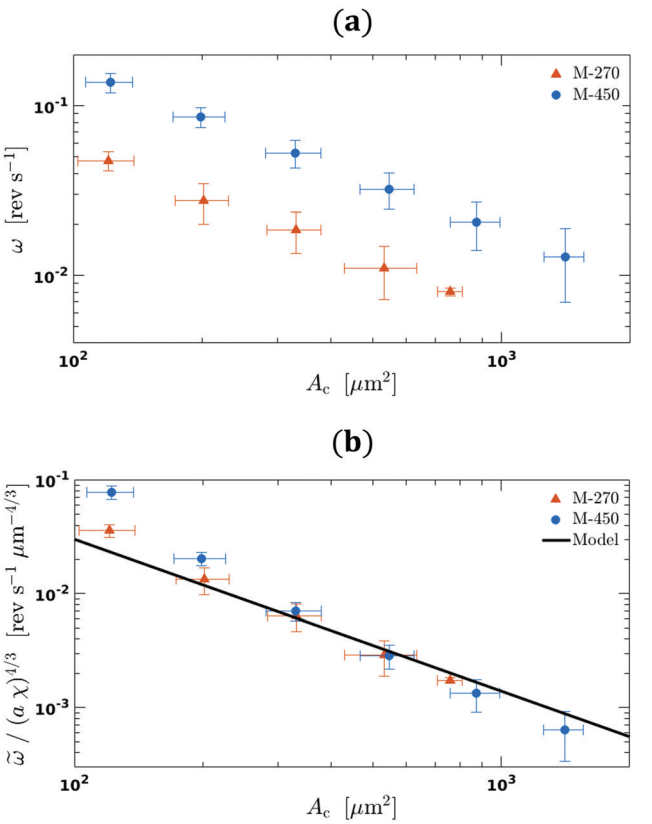

Fig. 4 (a) Cluster angular velocity ω as a function of cluster area A_c for Ω = 660 Hz, B = 1 mT for two different particle types, Dynabeads M-270 and M-450. (b) Normalized angular velocity $\tilde{\omega}/(a\chi)^{4/3}$ as a function of A_c. The continuous black line is a fit using eqn (4). Error bars are standard deviations over 5 experiments. The figure is obtained using the values of χ reported in the literature.[31] A version of the same figure using our direct experimental estimates of χ is shown in Fig. S2 in the ESI.†

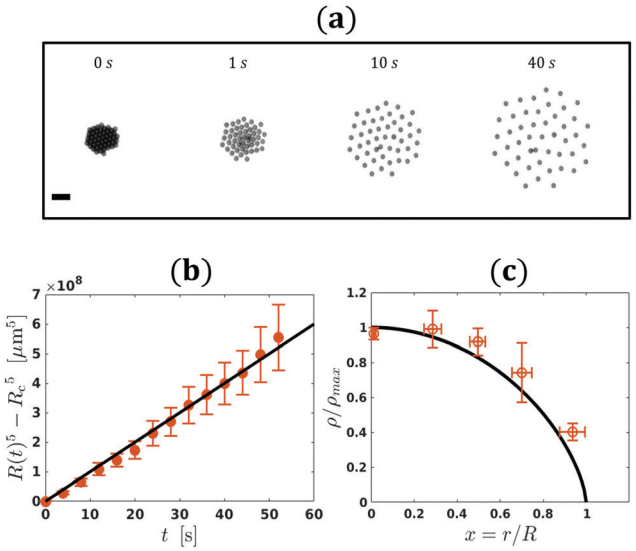

Fig. 5 (a) Experimental snapshots of the disassembly dynamics of a cluster of 47 particles (Dynabeads M-450). A constant, vertical magnetic field with B = 0.9 mT and θ = 0° is applied at t = 0. The scale bar corresponds to 20 μm. (b) Evolution of the cluster's size. Circles are experimental measurements and the black line is the prediction given by eqn (8). Error bars represent the uncertainty in measuring the cluster radius. (c) Density profile normalized by the maximal experimental density $\rho_{max}(t) \approx \rho_0(t)$ as a function of the normalized distance $x = r/R$, where R is the circle circumscribing the cluster. Circles represent averages over the 14 successive snapshots, with error bars representing standard deviations. The black line is the model's prediction, eqn (9).

mT (see also Supplementary Movie 2, ESI†). Fig. 5(b) shows an evolution of the cluster radius such that $R(t)^5$ increases linearly with t, as predicted by eqn (8). By fitting the experimental data we estimate a particle–substrate friction coefficient $\xi \approx 1.8 \times 10^{-7}$ Pa s m. This value is about 4 times larger than the friction coefficient due to the Stokes drag on a spherical particle, which indicates that substrate friction dominates over the hydrodynamic drag, as assumed in our model. The spatial dependence of the density profiles is shown in Fig. 5(c). As shown in the figure, the normalized density profiles at different times collapse into a master curve that is well described by our theoretical model, eqn (9). Overall, we conclude that our theoretical model of cluster disassembly provides an excellent description of both the spatial and temporal behaviors observed in the experiments.

5 Conclusions

We have investigated the rotation dynamics of disk-like paramagnetic particle clusters of different sizes and particle types in a precession magnetic field. Building on a previous study of the dynamics of 7-particle hexagonal clusters,[26] we have developed a theoretical model that links cluster rotation to its viscoelastic properties. Cluster rotation is driven by the magnetic torque and resisted by viscous friction. In the frequency range studied here, viscous friction prevents the cluster rotation from following the field. The cluster rotates at a slower frequency than that of the field, due to the emergence of an anisotropic line tension of magnetic origin. The combination of time-varying magnetic interactions and of an elastic resistance dominated by steric interactions makes the cluster behave as a viscoelastic material. Our theoretical model successfully describes the rotation dynamics and its dependence on cluster size, particle characteristics, and precession field frequency and strength. The model contains one single fitting parameter. By adjusting this parameter to the experimental data, we estimate the cluster viscoelasticity emerging in the rotation dynamics.

Upon switching the horizontal precession field into a vertical field, dipolar interactions become repulsive and the cluster disassembles. We explain the experimentally observed dynamics of cluster disassembly by a mean-field transport model. We obtain an exact, closed-form analytical solution, which describes the cluster's spatio-temporal density profile, in excellent agreement with the experiments. The theoretical model contains one single fitting parameter, which allows estimating the friction coefficient between particles and the substrate.

As discussed in the introduction, paramagnetic colloidal clusters are a dissipative self-assembled colloidal system that shares features with biological aggregates. In spite of the numerous differences with living matter, the shared physical features encourage us to project our findings onto future research directions in biophysical systems. The rotation of 2D isotropic magnetic clusters is reminiscent of spontaneous rotation observed in constrained 2D cell sheets,[37–39] the mechanisms of which are only partially understood. The same as the magnetic clusters, cell sheets are viscoelastic materials. Thus, travelling viscoelastic shear waves could be a mechanism at play in cell sheet rotation. Disassembly of magnetic clusters is reminiscent of the spread of tumoral cellular aggregates.[40] Indeed, tumor malignancy is linked to the epithelial-to-mesenchymal transition,[41] which enables cells to lose intercellular adhesion, escape from the tumor, and potentially initiate metastasis. This phenomenon bears resemblance with the switch from attractive to repulsive interactions that induce the disassembly of our magnetic clusters. This analogy suggests the possibility of transposing our mean-field theoretical description of magnetic cluster disassembly to describe the physics of the spread of certain types of tumor cells, by accounting for the appropriate biophysical interactions.

Author contributions

ME and LB performed the experiments, ME, HX and DGR developed the theoretical models, ME and DGR wrote the original draft, and all authors contributed to designing the study, analyzing the data and editing the manuscript.

Conflicts of interest

There are no conflicts to declare.

Acknowledgements

This work has been partially funded by the European Union through the program FEDER-FSE Lorraine et Massif des Vosges 2014–2020. We thank Mr Jean-Pierre Gobeau for his assistance in developing the experimental setup.

References

1 T. M. Hermans, H. Frauenrath and F. Stellacci, *Science*, 2013, **341**, 243–244.
2 B. G. P. van Ravensteijn, W. E. Hendriksen, R. Eelkema, J. H. van Esch and W. K. Kegel, *J. Am. Chem. Soc.*, 2017, **139**, 9763–9766.
3 S. A. P. van Rossum, M. Tena-Solsona, J. H. van Esch, R. Eelkema and J. Boekhoven, *Chem. Soc. Rev.*, 2017, **46**, 5519–5535.
4 V. Lijeström, C. Chen, P. Dommersnes, J. O. Fossum and A. H. Gröschel, *Curr. Opin. Colloid Interface Sci.*, 2019, **40**, 25–41.
5 N. Khalilgharibi, J. Fouchard, P. Recho, G. Charras and A. Kabla, *Curr. Opin. Cell Biol.*, 2016, **42**, 113–120.
6 D. Gonzalez-Rodriguez, K. Guevorkian, S. Douezan and F. Brochard-Wyart, *Science*, 2012, **338**, 910–917.
7 F. J. Vernerey, E. Benet, L. Blue, A. K. Fajrial, S. L. Sridhar, J. Lum, G. Shakya, K. H. Song, A. N. Thomas and M. A. Borden, *Adv. Colloid Interface Sci.*, 2019, **263**, 38–51.
8 U. Gasser, C. Eisenmann, G. Maret and P. Keim, *ChemPhysChem*, 2010, **11**, 963–970.
9 J. W. Tavacoli, P. Bauër, M. Fermigier, D. Bartolo, J. Heuvingh and O. Du Roure, *Soft Matter*, 2013, **9**, 9103.
10 C. P. Reynolds, K. E. Klop, F. A. Lavergne, S. M. Morrow, D. G. A. L. Aarts and R. P. A. Dullens, *J. Chem. Phys.*, 2015, **143**, 214903.
11 A. Darras, J. Fiscina, M. Pakpour, N. Vandewalle and G. Lumay, *Eur. Phys. J. E: Soft Matter Biol. Phys.*, 2016, **39**, 47.
12 R. Messina, S. Aljawhari, L. Bécu, J. Schockmel, G. Lumay and N. Vandewalle, *Sci. Rep.*, 2015, **5**, 10348.
13 L. Becu, M. Basler, M. L. Kulić and I. M. Kulić, *Eur. Phys. J. E: Soft Matter Biol. Phys.*, 2017, **40**, 107.
14 L. Spiteri, R. Messina, D. Gonzalez-Rodriguez and L. Bécu, *Phys. Rev. E*, 2018, **98**, 020601(R).
15 J. E. Martin and A. Snezhko, *Rep. Prog. Phys.*, 2013, **76**, 126601.
16 J. Abbott, *Rev. Sci. Instrum.*, 2015, **86**, 054701.
17 N. Osterman, I. Poberaj, J. Dobnikar, D. Frenkel, P. Ziherl and D. Babić, *Phys. Rev. Lett.*, 2009, **103**, 228301.
18 N. Casic, N. Quintero, R. Alvarez-Nodarse, F. G. Mertens, L. Jibuti, W. Zimmermann and T. M. Fischer, *Phys. Rev. Lett.*, 2013, **110**, 168302.
19 K. Müller, N. Osterman, D. Babič, C. N. Likos, J. Dobnikar and A. Nikoubashman, *Langmuir*, 2014, **30**, 5088–5096.
20 F. Martinez-Pedrero and P. Tierno, *Phys. Rev. Appl.*, 2015, **3**, 051003.
21 T. Mohorič, G. Kokot, N. Osterman, A. Snezhko, A. Vilfan, D. Babič and J. Dobnikar, *Langmuir*, 2016, **32**, 5094–5101.
22 H. Massana-Cid, F. Meng, D. Matsunaga, R. Golestanian and P. Tierno, *Nat. Commun.*, 2019, **10**, 2444.
23 K. J. Solis and J. E. Martin, *Soft Matter*, 2014, **10**, 9136–9142.
24 A. Snezhko, *Curr. Opin. Colloid Interface Sci.*, 2016, **21**, 65–75.
25 Y. Nagaoka, H. Morimoto and T. Maekawa, *Phys. Rev. E: Stat., Nonlinear, Soft Matter Phys.*, 2005, **71**, 032502.
26 P. Tierno, R. Muruganathan and T. M. Fischer, *Phys. Rev. Lett.*, 2007, **98**, 028301.
27 A. Weddemann, F. Wittbracht, B. Eickenberg and A. Hütten, *Langmuir*, 2010, **26**, 19225–19229.
28 B. H. McNaughton, K. A. Kehbein, J. N. Anker and R. Kopelman, *J. Phys. Chem. B*, 2006, **110**, 18958–18964.
29 S. L. Biswal and A. P. Gast, *Phys. Rev. E: Stat., Nonlinear, Soft Matter Phys.*, 2004, **69**, 041406.
30 J. Yan, S. C. Bae and S. Granick, *Soft Matter*, 2015, **11**, 147–153.
31 G. Fonnum, C. Johansson, A. Molteberg, S. Morup and E. Aksnes, *J. Magn. Magn. Mater.*, 2005, **293**, 41–47.
32 J. Schindelin, I. Arganda-Carreras, E. Frise, V. Kaynig, M. Longair, T. Pietzsch, S. Preibisch, C. Rueden, S. Saalfeld, B. Schmid, J.-Y. Tinevez, D. J. White, V. Hartenstein, K. Eliceiri, P. Tomancak and A. Cardona, *Nat. Methods*, 2012, **9**, 676–682.
33 H. Schlichting and K. Gersten, *Boundary-Layer Theory*, Springer, 1960.
34 L. L. Castro, G. R. R. Gonçalves, K. S. Neto, P. C. Morais, A. F. Bakuzis and R. Miotto, *Phys. Rev. E: Stat., Nonlinear, Soft Matter Phys.*, 2008, **78**, 061507.
35 A. V. Straube, A. A. Louis, J. Baumgartl, C. Bechinger and R. P. A. Dullens, *EPL*, 2011, **94**, 48008.
36 F. Martínez-Pedrero, J. Benet, J. E. F. Rubio, E. Sanz, R. G. Rubio and F. Ortega, *Phys. Rev. E: Stat., Nonlinear, Soft Matter Phys.*, 2014, **89**, 012306.
37 K. Doxzen, S. R. K. Vedula, M. C. Leong, H. Hirata, N. S. Gov, A. J. Kabla, B. Ladoux and C. T. Lim, *Integr. Biol.*, 2013, **5**, 1026.
38 M. Deforet, V. Hakim, H. G. Yevick, G. Duclos and P. Silberzan, *Nat. Commun.*, 2014, **5**, 3747.
39 M. J. Siedlik, S. Manivannan, I. G. Kevrekidis and C. M. Nelson, *Biophys. J.*, 2017, **112**, 2419–2427.
40 S. Douezan, K. Guevorkian, R. Naouar, S. Dufour, D. Cuvelier and F. Brochard-Wyart, *Proc. Natl. Acad. Sci. U. S. A.*, 2011, **108**, 7315–7320.
41 J.-P. Thiery, *Curr. Opin. Cell Biol.*, 2003, **15**, 740–746.
42 A. Spatafora-Salazar, D. M. Lobmeyer, L. H. P. Cunha, K. Joshi and S. L. Biswal, *Soft Matter*, 2021, **17**(5), 1120–1155.